# Multiple Diffusion Pathways in Pluronic F127 Mesophases Revealed by Single Molecule Tracking and Fluorescence Correlation Spectroscopy

Alec W. Kirkeminde, Travis Torres, Takashi Ito, and Daniel A. Higgins*

Department of Chemistry, Kansas State University, Manhattan, Kansas 66506-0401, United States

S *Supporting Information*

ABSTRACT: Single molecule tracking (SMT) and fluorescence correlation spectroscopy (FCS) are used to investigate probe molecule diffusion within the mesophase structures of Pluronic F127 gels. Mixtures are prepared in the hexagonal, lamellar, and cubic regions of the ternary F127/water/butanol phase diagram and are doped with nanomolar concentrations of a perylene diimide dye (DTPDI). Flow aligned F127 gels comprised of hexagonally arranged cylindrical micelles exhibit distinct one-dimensional (1D) DTPDI motion in wide-field videos, with diffusion occurring parallel to the flow alignment direction. The slow 1D dye motion observed is attributed to single molecule diffusion within the viscous, hydrophobic micelle cores. FCS data acquired from the same samples reveal a bimodal distribution of diffusion coefficients with the slower component assigned to 1D motion in the micelle core and the faster component to 3D diffusion in the interconnected micelle coronas. The rate of diffusion for both components increases with decreasing F127 concentration, reflecting a decrease in gel microviscosity. SMT data from the lamellar and cubic mesophases depict isotropic 2D and 3D diffusion, respectively, and provide supporting evidence for the role of the micelle core and corona in governing diffusion. Trajectory angle distributions from 1D diffusing species in the hexagonal mesophase provide quantitative information on the alignment of the cylindrical micelles. These results, and the rare observation of misaligned trajectories, indicate the hexagonal phase is highly ordered.
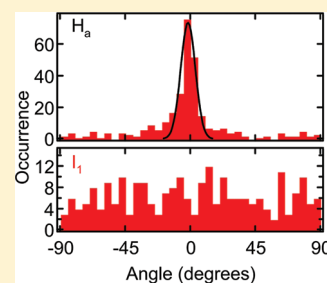
INTRODUCTION

Single molecule tracking (SMT) and fluorescence correlation spectroscopy (FCS) are now being widely employed to study molecular diffusion within lipid layers,[1−6] at surfaces and interfaces,[7−14] in mesoporous silica,[15−24] hydrogels,[25,26] single crystals,[27] and small-molecule thermotropic liquid crystals.[28,29] A primary objective of many of these studies has been to better understand the role played by local materials structure in governing molecular mobility.[2,6,30] For example, Moerner and co-workers recorded single molecule trajectories within cracks formed in spin-grown *p*-terphenyl crystals to probe crack structure and the mechanism of dye diffusion.[27] Likewise, in recent work by the Brauchle group[15−18] and others,[19,24] SMT has been employed to investigate molecular diffusion within the nanochannels formed in mesoporous silica films. Such studies provide the means to assess silica nanochannel connectivity,[31] and local nanochannel alignment.[24] Both are of particular importance for the development of efficient nanoporous membranes and filters incorporating well-aligned nanochannels.[32−35]

While the "solid" structures (i.e., silica nanochannel walls) in the above materials provide a clear mechanism for guiding molecular motion (i.e., impermeability), there is also strong interest in understanding how the much more "diffuse" structures of lyotropic liquid crystalline mesophases may limit and control molecular diffusion.[36−39] When dissolved in water at high concentrations, the nonionic triblock copolymer surfactants known as "Pluronics" form a broad range of mesophases that yield such interesting properties. The Pluronics are comprised of a relatively hydrophobic poly(propylene) oxide (PPO) block positioned between two relatively hydrophilic poly(ethylene) oxide (PEO) blocks. Figure 1 depicts the chemical structure of one such polymer, Pluronic F127. The aqueous mesophases formed by F127 and related nonionic surfactants depend on polymer concentration,[40] ambient temperature[41] (many form thermoreversible gels),[42] and the presence of cosolvents.[40,43] Mesophase organization in these systems has been widely studied by optical microscopy[36,37,44,45] and spectroscopy,[41,43,46] cryo-transmission electron microscopy (TEM),[47] small-angle X-ray[37,40,44,45] and neutron[48,49] scattering, and by NMR spectroscopy.[40,46,50,51]

X-ray and neutron scattering have revealed a wealth of knowledge on static mesophase structure[40,52] and on the degree of alignment produced by flow fields.[33,44,45,49] However, the information obtained largely depicts average material properties. Although TEM provides the high-resolution necessary to visualize materials structure,[47] it yields no data on dynamic phenomena such as probe partitioning and diffusion. Dynamics within such mesophases have been investigated by NMR relaxation[46,51] and pulsed field gradient methods,[50] providing valuable data on
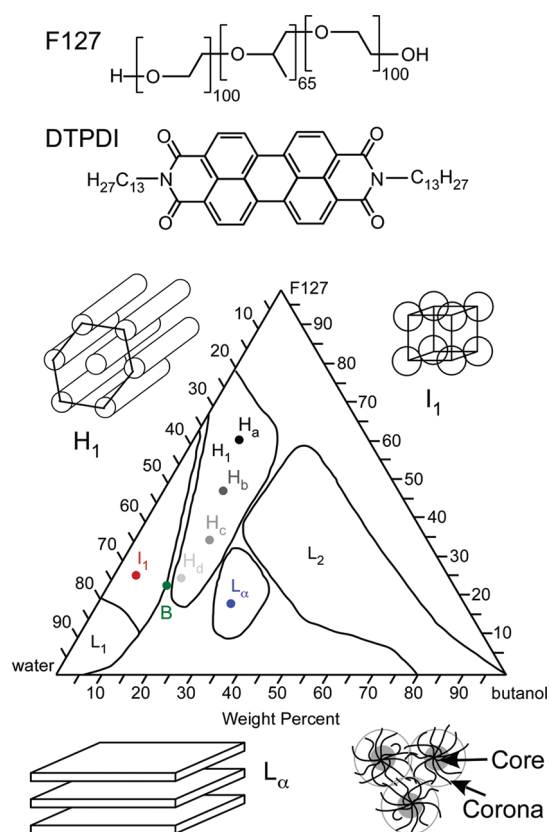
Figure 1. (Top) Chemical structure of Pluronic F127, a triblock copolymer comprised of poly(ethylene oxide) and poly(propylene oxide) blocks. Also shown is the structure of the perylene diimide (DTPDI) dye used. (Bottom) Phase diagram for F127/water/butanol mixtures, modified from ref 40. Shown are the normal hexagonal (H_1), isotropic (I_1), and lamellar (L_α) regions investigated, along with the normal (L_1) and reverse (L_2) micellar regions. The filled circles appended to H_1, I_1, and L_α regions depict the samples prepared and characterized. The diagrams at the upper left, upper right, and lower left show simple models for assembly of copolymer molecules in each phase. The diagram at the lower right depicts the core and corona regions of cylindrical and spherical micelles.

Table 1. Ternary F127 Gel Compositions (in wt %), as Designated in Figure 1[a]

	H_a	H_b	H_c	H_d	I_1	B	L_α
F127	60.7	47.5	34.8	24.9	26.4	22.7	18.0
water	29.0	38.6	48.3	59.9	68.5	63.7	52.1
butanol	10.3	13.9	16.9	15.2	5.1	13.6	29.9

[a] All contain DTPDI dye at a concentration of 5 nM.

To this end, a series of dye-doped F127/water/butanol mixtures in three different regions of the ternary phase diagram were prepared and characterized. The hexagonal mesophase was emphasized in these investigations because it affords a simple route to flow aligned materials[33,44,45] in which probe diffusion along specific structures can be directly visualized. A hydrophobic dye, N,N'-bis(tridecyl)-perylene-3,4,9,10-tetracarboxylic diimide (DTPDI, see Figure 1) was selected as the probe because of the expectation that it would partition into the hydrophobic cores of the F127 micelles. SMT results from flow aligned hexagonal gels depict slow 1D dye diffusion along the flow alignment direction, and are concluded to reflect dye motion within the micelle core. The distribution of 1D trajectory orientations is attributed to the presence of highly ordered cylindrical micelles. FCS results from these same samples depict a bimodal distribution of diffusion coefficients, consistent with partitioning of the dye between (and motion within) the core and corona. The two diffusing populations afford important measures of the microviscosity within these regions. Results obtained for 2D diffusion in lamellar phases and 3D diffusion in cubic gels indicate that probe diffusion is impacted by the complex domain structure in the latter, while the lamellar phase exhibits more uniform properties. The detailed mechanisms of diffusion through mesophase structures in this class of lyotropic liquid crystals are of direct relevance to their use as chemical separations media[54,55] and in drug delivery.[55]

■ EXPERIMENTAL CONSIDERATIONS

F127 Gels. The triblock copolymer Pluronic F127 was obtained from Anatrace and was used as received. Figure 1 depicts the structure of F127, which has the formula $PEO_{100}PPO_{65}$-PEO_{100}. Water (HPLC grade) and n-butanol (reagent grade) used in preparation of F127 gels were obtained from Sigma Aldrich.

Solutions were prepared in several different regions of the ternary F127/water/butanol phase diagram. These are depicted on the phase diagram shown in Figure 1. They include four different mixtures falling within the hexagonal region (designated as H_a, H_b, H_c, and H_d), one solution in the cubic region (I_1 in Figure 1), one on the cubic/hexagonal phase boundary (B) and one in the lamellar phase (L_α). The exact solution compositions used in each are given in Table 1. A common procedure was used to prepare all samples. In this process, F127 was first weighed and transferred into a disposable glass vial. Appropriate amounts of n-butanol and water were then added. In dye-doped F127 solutions, a fraction of the n-butanol was replaced by a dilute ethanolic solution of the dye. The vial was immediately sealed and the solution mixed by repeatedly inverting and centrifuging. All but the L_α solution formed high viscosity gels that did not flow under gravity alone. These gels also entrapped large numbers of air bubbles after mixing. The bubbles were removed by centrifuging for several hours over the course of two days. Incorporation

the rate and anisotropy of self-diffusion and tracer diffusion. However, neither allows for direct visualization of molecular motions and both involve averaging of signals from a large number of probe species. Optical measurements on the Pluronics and related materials have been used to investigate both the rotational[38] and translational diffusion[36,37,39] of dissolved fluorescent probes, along with their static spectroscopy.[41,46,53] Comparison of results obtained using polar and nonpolar probes[39] has offered important evidence of the roles played by the micelle core and corona regions in governing molecular mobility.[41,46,53] However, much remains to be learned about the molecular level details of how these structures support, facilitate, and control probe diffusion. For example, the exact phases through which probe molecules diffuse have not yet been directly observed to our knowledge. Rather, diffusion within the core and corona has only been inferred by use of dyes deemed to preferentially partition into each phase.

In this paper, we employ SMT and FCS methods as means to better understand the role of mesophase structures in governing probe molecule diffusion through ordered and flow aligned F127 gels.

of waiting times between centrifugation periods led to bubble coalescence and aided in their removal. The gels were stored sealed, in the dark, for a period of at least two days prior to use.

DTPDI was obtained from Sigma Aldrich and was used as received. Its structure is shown in Figure 1. A 96 nM ethanolic (HPLC grade) solution of the dye was used to prepare dye doped F127 samples. In each case, a 100 μL aliquot of dye solution was added to the F127 solution, yielding a final dye concentration of ∼5 nM.

Flow Alignment of Gels. Microfluidic channels used for encapsulation and flow alignment of the F127 samples were prepared by casting uncured poly(dimethylsiloxane) (PDMS, Sylgaard 184) in a prefabricated glass mold. This mold was designed to form rectangular PDMS monoliths of 1.5 mm thickness, 2.5 cm length, and 1.2 cm width. An open, rectangular microfluidic channel of 0.5 mm depth, 2.5 mm width, and 15 mm length was templated in the PDMS monolith by inclusion of a short rectangular capillary (Vitrocom) in the mold. Once cured and removed from the mold, 1.5 mm diameter inlet and outlet holes were punched in the ends of the channel. The PDMS monolith was subsequently cleaned in an air plasma (5 min) along with a microscope coverslip (FisherFinest Premium). The PDMS monolith and coverslip were then pressed together to form a PDMS based microfluidic channel in which the microscope coverslip formed the bottom surface of the channel. All optical experiments involved imaging through the coverslip.

F127 gels were loaded into the channels by first drawing the gel into a short glass capillary using a syringe pump. The capillary was then contacted to the channel inlet and the syringe pump reversed to infuse the gel into the channel. Viscous gels in the hexagonal and cubic regions of the phase diagram were flowed into the channels at a linear flow velocity of ∼0.5 mm/s. The small dimensions of the channel and the extremely high viscosities of the gels ensure that loading of the channel occurred within the laminar flow regime. Optically clear gels were obtained in all cases. After filling, the inlet and outlet holes were sealed using standard, two-part 5 min epoxy. All samples were characterized within a few hours of preparation. The ambient temperature during sample characterization ranged from 20 to 22 °C.

Optical Microscopy. All SMT experiments were performed in total internal reflection fluorescence (TIRF) mode on a wide-field fluorescence microscope.[24] This system is built upon an inverted epi-illumination microscope (Nikon TiE) and employs closed-loop focus stabilization. Light from a blue diode laser (488 nm) was used to excite dye fluorescence. It was first focused into a spinning optical diffuser and then collected, reflected from a dichroic beamsplitter (Chroma, 505 DCLP) and focused, off-axis, into the back aperture of an oil immersion objective (Nikon Apo TIRF 100X, 1.49 numerical aperture, NA). The incident laser power was maintained between 1 and 2 mW. Fluorescence from the sample was collected and directed back through the dichroic beamsplitter, through a bandpass filter (Chroma HQ535/50 m) and onto the photosensitive surface of a back-illuminated electron multiplying CCD (EM-CCD) camera (Andor iXon DU-897). Pixel size in the images was found to be 62.5 nm by calibration using 1.0 μm diameter fluorospheres (Invitrogen).

The refractive index of one F127 gel (H$_b$, Figure 1) was measured to be 1.43, giving an evanescent wave penetration depth (1/e) in the sample of ∼185 nm with the 1.49 NA objective. TIRF videos were typically acquired at frame rates of 2−8 frames per second for a total length of 200−300 frames.

Primary image analysis, spot detection, and trajectory generation were accomplished using the freely available ImageJ software and a particle tracking plugin.[56] Initial visualization of the 1D trajectories followed by probe molecules in the hexagonal phase was achieved using the "z-project" routine within ImageJ.

All FCS measurements were performed on a home-built sample scanning confocal microscope.[57] The laser and optical filters employed were mostly identical to those used in TIRF experiments. In this case, a 1.3 NA oil immersion objective (Nikon Plan Fluor, 100×) was employed. This objective produced a nearly diffraction limited focus in the gel, ∼1−2 μm above the coverslip interface. The incident laser power was maintained at ∼7 μW. An appropriate notch filter was employed along with the dichroic and bandpass filters noted above. A single-photon-counting avalanche photodiode was used as the detector. Data were collected with bin times ranging from 1 to 5 ms. Detection volume dimensions were determined for accurate measurement of diffusion coefficients by filling the PDMS microfluidic channel with a dilute aqueous suspension of 100 nm diameter fluorospheres (Duke). Time transients acquired from these samples were treated in a manner identical to those from dye doped F127 samples (see below).

■ RESULTS AND DISCUSSION

As the primary objective of this work is to explore the role of gel structures in governing probe molecule diffusion, the majority of experiments were performed on aligned F127 hexagonal mesophases, where single molecule diffusion within identifiable gel structures could readily be visualized. The hexagonal F127 mesophase is comprised of ordered cylindrical micelles[40] (see Figure 1) that are easily aligned by flow.[33,44,45] Four different gel concentrations (designated H$_a$−H$_d$) were used to explore the influence of F127 concentration on probe molecule diffusion, sample microviscosity, the appearance of 1D molecular motion, and as an extension, the degree of micelle alignment. The results were compared to those of the cubic (I$_1$) and lamellar (L$_\alpha$) mesophases. No investigations of other phases (i.e., L$_1$ and L$_2$, normal and inverse isotropic micellar phases, respectively)[40] were undertaken.

Single Molecule Tracking. TIRF mode[58] was employed for collection of wide-field videos depicting single molecule diffusion in the F127 gels. Its use was deemed necessary to minimize background fluorescence from molecules at different depths.[58] These images are therefore limited to regions within ∼200 nm of the gel/glass interface, as governed by the decay of the evanescent fields from this interface. All videos acquired show a predominance of mobile molecules and a small minority of immobile molecules. The latter are attributed to adsorption of some molecules at the coverslip surface; they are excluded from further analysis as discussed below.

Figure 2a depicts a representative TIRF image (produced by combining all 200 frames from a single video) showing the motions of individual DTPDI molecules in an H$_b$ F127 gel. The original video is provided as Supporting Information. A predominance of 1D molecular motion is clearly observed. Nearly indistinguishable results were obtained from H$_a$ and H$_c$ gels, while little, if any, 1D motion was ever observed in gels of H$_d$ composition (see Figure 1). Collection and inspection of a large number of replicate videos (∼100) from different locations in different H$_a$−H$_c$ samples clearly demonstrate that most mobile DTPDI molecules (>1000 have been observed) follow 1D paths.
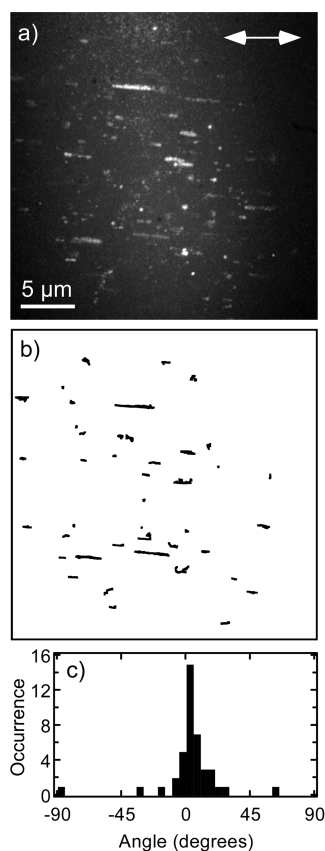
Figure 2. (a) Fluorescence image depicting the combined frames of a 200 frame wide-field video recorded at 3 frames/s showing DTPDI motions in a flow-aligned H_b F127 mixture (Figure 1). (b) Single molecule trajectories reflecting a predominance of one-dimensional (1D) diffusion of DTPDI molecules in flow-aligned hexagonal F127 gels. The trajectories shown were obtained from the video in (a). (c) Histogram showing the trajectory angles from (b), obtained by a previously reported orthogonal regression analysis. The expected alignment is along the horizontal direction (0°) on the image (see arrow).

Figure 3. (a) Ensemble MSD data (symbols) from SMT experiments performed on samples at the designated points on the F127/water/ butanol phase diagram. All frame times were 0.36 s, except for the H_c data in which it was 0.16 s. A total of 52, 93, 25, and 78 trajectories were employed to obtain the plots shown for H_a, H_b, H_c, and I_1, respectively. Error bars depict the standard deviation about the mean in each. Also shown are linear fits (solid lines) to these data. (b) Histogram depicting the mean values of the diffusion coefficients and 90% confidence intervals (error bars) obtained from individual single molecule trajectories ≥7 frames in length for videos recorded at a range of frame rates.

Importantly, the 1D motions observed were found to be parallel to the flow alignment direction in the vast majority of cases. As the only 1D structures present in these materials are cylindrical F127 micelles, it is concluded that the micelles play a direct role in guiding molecular motion. The observation of 1D motion and the intensity of single molecule emission show no dependence on the incident polarization state, consistent with rapid tumbling of the molecules as they move through the gel.[39,59]

A more detailed analysis of single molecule motion was accomplished by linking the fluorescent spots in the individual video frames into trajectories. Automated software routines were used for this purpose.[56] Figure 2b plots trajectories from the video in Figure 2a. Only those trajectories ≥7 frames in length are shown, and only these trajectories are used in subsequent analyses. As is readily apparent, most (but not all) of the 1D "streaks" shown in Figure 2a produce 1D trajectories in Figure 2b. The differences arise primarily from limitations of the tracking procedure, which can only be used to link images of relatively slow-moving molecules, namely, those moving fewer than ~6 pixels between frames in the present case.

Orientations of the individual trajectories were determined by fitting each to a line, using previously described orthogonal regression
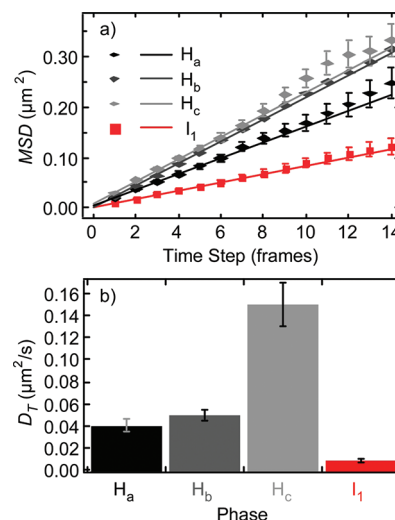
methods.[24] Again, immobile molecules were excluded from the analysis. A histogram plotting the (in plane) orientation angles of the trajectories in Figure 2b is shown in Figure 2c. The histogram data provide a direct means for observing the alignment of the trajectories and the spread of trajectory angles. The peak of the histogram closely corresponds to the flow alignment direction, which was along the 0° (±5°) direction. These results and similar data from ~100 videos recorded in H_a−H_c samples lead to the qualitative conclusion that all such samples exhibit very well aligned 1D diffusion of DTPDI. In the case of H_d, most molecular motion was concluded to be too fast to directly observe. A quantitative discussion of materials order is given below.

The data on molecular position comprising the trajectories provides the means to determine a diffusion coefficient, D, for each molecule.[1] Such information is obtained by plotting mean square displacement, MSD, as a function of time, t, and fitting these data to the expected linear function; that is, MSD = $2nDt$ for n-dimensional motion. Nonlinearities observed in these plots can reflect the presence of confining structures.[2] However, single molecule results often exhibit such nonlinearities on all but short time scales due simply to random fluctuations in the diffusion pathway.[21,60] More reliable information on longer time scales can be obtained by combining the single molecule results to access ensemble averaged MSD data. Figure 3a shows ensemble plots from H_a−H_c samples, with error bars calculated by the method of Qian, et al.[60,61] The data shown are from trajectories ≥16 frames in length. Lines fit through the first four data points (see Figure 3a) in each fall within the error bars, demonstrating the Brownian nature of 1D molecular motion on several-second time scales, and ~0.5 μm length scales in these samples. These same ensemble data provide strong evidence that the nonlinearities observed in single molecule MSD plots result from random fluctuations in the diffusion pathways alone. Were confining

Table 2. Diffusion Coefficients, D_T, from SMT Experiments, and D_s and D_f from FCS, in $\mu m^2/s$[a]

	H_a	H_b	H_c	H_d	I_1	B	L_α
D_T	0.041 ± 0.006	0.050 ± 0.005	0.15 ± 0.02		0.009 ± 0.002		
η_T	5300	4300	1500		23000		
D_s	0.20 ± 0.10	0.65 ± 0.25	0.78 ± 0.37	1.9 ± 1.0	0.23 ± 0.07	0.19 ± 0.13	
η_s	1100	330	280	120	930	1100	
D_f	6.8 ± 1.1	15 ± 1	13 ± 2	28 ± 6	12 ± 3	17 ± 2	29 ± 8
η_f	32	14	16	7.6	18	13	7.4

[a] Also provided are the 90% confidence intervals (error bars) and apparent microviscosities, η, in cP (20−22 °C) obtained from SMT and FCS experiments.

structures present, the ensemble MSD plots would also be expected to deviate from linearity.

As single molecule data yield reliable measurements of D on short time scales,[21] data obtained from trajectories ≥7 frames in length were fit in a similar fashion (over four frames) to determine single molecule D values for the H_a−H_c samples. The mean values are given in Table 2 (listed as D_T) and are plotted in Figure 3b. Immobile molecules in the associated videos were determined to exhibit a noise-limited localization variance[24] of 0.25 pixels[2]. Therefore, only those molecules exhibiting a frame-to-frame MSD > 0.5 pixels[2] were classified as "mobile" and included in this analysis.

It should be noted that the SMT data provides only a "lower-limit" estimate of single molecule diffusion coefficients in the F127 gels. The values obtained reflect only the slowest molecular motions. The need to acquire data from relatively large sample regions while avoiding image pixilation, coupled with the limited brightness of DTPDI, required that video rates of ≤8 frames/s be employed. With a maximum frame−frame displacement of ∼6 pixels (375 nm) for spot linking, the maximum measurable diffusion coefficient, D_{max}, is estimated ($MSD_{max} = 2D_{max}t$) to be ∼0.5 $\mu m^2/s$. Faster moving molecules are not linked into trajectories and thus are not included in the analysis, depressing D. Videos recorded at different frame rates show a clear frame-rate dependence in the D values (see Figure 3), consistent with this type of bias. However, the observed average length of trajectories employed (12−14 frames) should be sufficient to avoid significant bias due to statistical factors alone.[60] Trajectory length is limited by tracking difficulties, escape of the dye from the micelle core and photobleaching. As all three mechanisms lead to trajectory termination, it is not possible at present to determine the cause of each such event. The frame-rate dependence observed in the D values is concluded to primarily reflect biased tracking of molecules exhibiting a range of D values, rather than errors due to limited measurement statistics.

The apparent microviscosities (i.e., upper-limit estimates) determined from the Stokes−Einstein equation (assuming a 1 nm dye radius) are presented in Table 2 (as η_T, in cP). It is clear that the environments producing 1D molecular motions are of very high microviscosity. As will become apparent below, these are some of the highest viscosity environments found within the present F127 samples. The observation of slow 1D diffusion is therefore concluded to arise from molecular motion within the core of the cylindrical micelles comprising the hexagonal mesophase. Figure 1 includes a diagram depicting the core and corona regions. The core region has been shown previously to exhibit very high microviscosities.[39,53,59] The corona regions form a less viscous, continuous phase that is instead expected to support 3D dye motion.[40,48,49]

Interestingly, the D values obtained (Table 2, D_T) are 1−2 orders of magnitude smaller (and the microviscosities correspondingly higher) than previously reported for similar F127

materials and different dyes.[39,59] While some of this difference results from measurement bias (see above), it is consistent with the presence of very high viscosity domains associated with local fluctuations in the F127 (e.g., PPO) concentration in the micelle core.[48] Indeed, the three trackable hexagonal samples (H_a−H_c) exhibit a clear monotonic trend toward increasing D with decreasing F127 concentration (see Figure 3 and Table 2). The associated concentration-dependent decrease in the microviscosity of the micelle core is consistent with literature results,[53] and supports the above interpretation of the anomalously small D values.

Wide-field TIRF videos were also acquired from lamellar (L_α), cubic (I_1), and cubic/hexagonal boundary (B) samples (see Figure 1). These videos show motions consistent with 2D (L_α) and 3D (I_1 and B) diffusion for mobile molecules. Representative videos are provided as Supporting Information. Mobile molecules found in the lamellar region moved too rapidly to be tracked and have not been analyzed. Those in the cubic phase and in the boundary region exhibit much slower motions and can easily be followed. Figure S1 depicts trajectories from a representative video of a cubic sample. Although this sample clearly exhibits 3D diffusion,[25] the trajectories have been analyzed in 2D to allow for easy visualization and comparison of trajectory angles with the hexagonal phase data (see below). As with the hexagonal samples, the cubic region also provides evidence of Brownian dye motion on short time scales (see Figure 3a). DTPDI diffusion coefficients from the I_1 sample are also given in Figure 3b and Table 2. This sample exhibits the highest microviscosity of all samples investigated by SMT. DTPDI mobility in the cubic phase most likely reflects long-term confinement of the dye to the micelle core and slow diffusion of the micelles themselves.

Fluorescence Correlation Spectroscopy. As described above, DTPDI molecules exhibiting 1D motion are clearly located within the F127 micelle core in the hexagonal mesophase. However, it is obvious the molecules also partition between the core and corona regions. Once a molecule exits the core, its diffusion coefficient is expected to increase dramatically, to the point where the molecule can no longer be tracked as a single entity and effectively "disappears". This expectation, coupled with the realization that some DTPDI molecules within the F127 micelles move faster than can be easily followed by SMT led us to also characterize all samples by FCS methods. For these experiments, single point time transients ($i(t)$, ∼10 min in length) were acquired from multiple regions within each sample. The normalized autocorrelation function, $C(\tau)$, for each transient was then calculated as follows:

$$C(\tau) = \frac{\langle i(t)i(t+\tau)\rangle}{\langle i(t)\rangle^2} - 1 \tag{1}$$

Figure 4a shows representative autocorrelation data from four different regions within the F127/water/butanol phase diagram.

12740

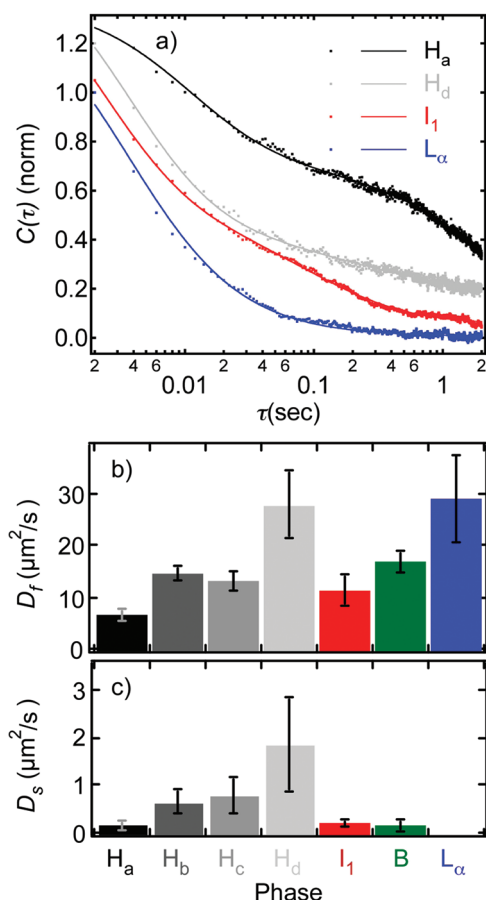dx.doi.org/10.1021/jp208234b |*J. Phys. Chem. B* 2011, 115, 12736–12743

Figure 4. (a) Representative autocorrelation data (dots) from FCS experiments on samples at the designated points on the F127/water/butanol phase diagram. Also shown are fits (solid lines) to appropriate models of each decay (see text). With the exception of the L_α region, all samples investigated required two component models to properly fit the decay. Data have been offset for easy visualization. (b, c) Histograms depicting the mean diffusion coefficients and 90% confidence intervals (error bars) obtained from FCS studies in seven different samples.

Each region shows fundamentally different behavior, associated with its specific structure.

Autocorrelation data from the hexagonal mesophase shows clear evidence of separate fast and slow components in each decay (see Figure 4a, traces H_a and H_d). Diffusion coefficients were extracted from these data by fitting to a carefully selected two-component model for the decay. Based on the SMT data above, a term modeling 1D diffusion was included to fit the slow decay component. The second term models fast, 3D diffusion expected for dye molecules found within the continuous hydrophilic corona region. The full fitting expression used for data from the hexagonal mesophase is as follows:[62,63]

$$G(\tau) = \frac{A}{(1 + \tau D_f/\sigma^2)\sqrt{1 + \tau D_f/z^2}}$$
$$+ \frac{B}{\sqrt{1 + \tau D_s/\sigma^2}} + C \qquad (2)$$

where A, B, and C are fitting constants, D_f and D_s are the diffusion coefficients (also fitting constants) for the fast and slow decays, respectively, and σ and z represent the lateral and longitudinal

detection volume dimensions (calibrated as described under Experimental Considerations).

Figure 4b,c and Table 2 give the mean diffusion coefficients measured in the four different hexagonal samples ($H_a - H_d$). The two diffusion coefficients obtained from FCS data differ from each other by approximately 1 order of magnitude. The D_s and D_f values obtained were found to be invariant within experimental error for FCS data acquired using 1, 2, and 5 ms bin times. These values and the calculated microviscosities (see Table 2) closely match those determined from fluorescence anisotropy measurements,[59] studies of environment-dependent quantum yields and Stokes shifts,[53] and FCS studies[39] of related materials. The faster, 3D component yields D_f values ranging from 6.8 to 28 $\mu m^2/s$ that increase with decreasing F127 content. Attempts to fit the data to a two-component 1D model produced physically unrealistic diffusion coefficients ($\sim 10^2 - 10^3$ $\mu m^2/s$) for the fast component. The slower 1D component yields D_s values between 0.2 and 1.9 $\mu m^2/s$ that are approximately 10-fold larger than from SMT data. These values also increase as the F127 concentration decreases.[53] The differences observed between the SMT data and the slow component of the FCS data again reflect experimental bias in the SMT data, but also suggest the microviscosity of the micelle core is highly variable. Widely variable diffusion coefficients have been observed previously in similar materials by NMR[50] and by optical methods.[59]

For purposes of comparison with the hexagonal region, FCS data were also acquired in the cubic (I_1) and lamellar (L_α) mesophases, as well as in the cubic-hexagonal boundary region (B). As noted above, videos and SMT data from these samples depict the expected behavior, namely, 2D and 3D diffusion. FCS data from the lamellar phase could be fit to a single-decay model for 2D diffusion:

$$G(\tau) = \frac{A}{1 + \tau D/\sigma^2} + B \qquad (3)$$

Diffusion in this region was relatively fast, yielding the largest D values observed (see Figure 4b and Table 2). The fitting of these data to a single component model was somewhat unexpected as the lamellar phase also incorporates hydrophobic PPO and hydrophilic PEO regions (see Figure 1). Incorporation of significant quantities of butanol ($\sim$30% by wgt), coupled with the expectation that the butanol preferentially solvates the hydrophobic region of the mesophase,[40] suggests that the viscosity of the PPO layers is greatly reduced, relative to that of the hexagonal mesophase. Thus, two-component diffusion may be masked in the lamellar phase by similar microviscosities in hydrophilic and hydrophobic regions.

The occurrence of two component diffusion, and the importance of the hydrophobic domains in governing slow diffusion is further evidenced by results from the cubic mesophase, which is known to be comprised of tightly packed spherical micelles (see Figure 1).[48] In this case, the autocorrelation data was fit to a model incorporating two components for 3D diffusion:

$$G(\tau) = \frac{A}{(1 + \tau D_f/\sigma^2)\sqrt{1 + \tau D_f/z^2}}$$
$$+ \frac{B}{(1 + \tau D_s/\sigma^2)\sqrt{1 + \tau D_s/z^2}} + C \qquad (4)$$

It is noteworthy that the difference in the D_f and D_s values for fast and slow diffusion was greatest in this region (see Figure 4 and Table 2). The butanol content in this case was the smallest of
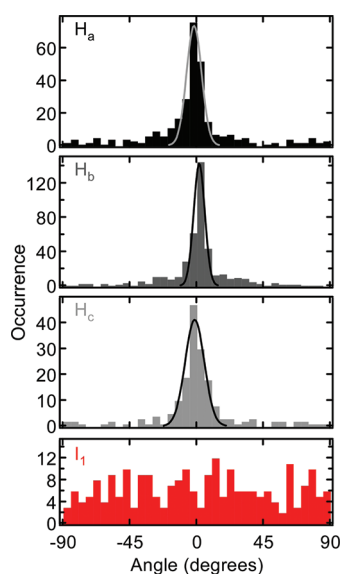
Figure 5. Histograms depicting the distributions of trajectory angles from wide-field videos recorded in the designated samples. Trajectory angles were obtained by a previously reported orthogonal regression analysis. Highly aligned, well ordered cylindrical micelles are found in the hexagonal region, while the isotropic region (I_1) depicts the complete absence of oriented diffusion, as expected.

all samples investigated, suggesting formation of highly distinct hydrophobic and hydrophilic domains of significantly different properties. Data from the boundary region yield values intermediate to those of the hexagonal (H_d) and cubic phases. As noted above, a likely model for slow diffusion in the cubic region involves long entrapment of the dye within the micelle core, coupled with slow self-diffusion of the micelles. Fast diffusion is again assigned to DTPDI motion in the corona region.

Orientational Order in the Hexagonal Mesophase. The 1D trajectories exhibited by DTPDI molecules within the flow aligned hexagonal mesophase provide a means for quantitative characterization of the alignment and orientational order of the cylindrical micelles. In a recent study,[24] we described the use of orthogonal regression[64−66] procedures for the determination of 1D trajectory angles from molecules diffusing through "polycrystalline" mesoporous silica films. The individual trajectory angles were used to construct histograms depicting domain alignment and orientational order (i.e., the spread of alignment angles) and to calculate quantitative order parameters reflecting materials order. Unfortunately, it was not possible to align the domains along any particular direction by the spin coating methods employed.[24] In the F127 hexagonal mesophase, such alignment is readily induced by gel flow.[45] Figure 2c depicts the histogram of trajectory orientations for the trajectories shown in Figure 2b. The same procedure has been employed to characterize trajectory alignment in several H_a, H_b and H_c samples. Figure 5 presents histograms depicting the results (mobile molecules only). For comparison purposes, data from the I_1 sample is also shown. Note that the trajectory angle is strictly undefined in the latter. However, the relatively short time over which the molecules can be tracked results in the fortuitous observation of "anisotropic" trajectories (i.e., each can be fit to a line).[24] These data show that such trajectories are, on average, randomly aligned, as expected, in the cubic sample.

For the H_a, H_b, and H_c samples, the trajectory angle distributions show clear evidence of alignment along the expected direction

(i.e., $0 \pm 5°$). Some angular uncertainty arises from the imprecision of sample alignment on the microscope. The spread in trajectory angles also depicts a high degree of micelle orientational order in each. The average tilt angles, determined from fits of the histograms to Gaussian functions are found to be 5.1, 3.7, and 6.4° for the H_a, H_b, and H_c samples, respectively. Defining the relevant order parameter as $\langle P \rangle = 2\langle \cos^2\theta \rangle - 1$, these data yield $\langle P \rangle = 0.98, 0.99$, and 0.97, respectively, while the noise-limited maximum measurable order parameter is ~0.998.[24] While the order parameter employed is the 2D analog of the usual second Legendre Polynomial,[67] its use is justified by the rectangular channel geometry and the relatively long (compared to common small molecule liquid crystals) cylindrical micelles comprising the sample. Determination of $\langle P \rangle$ from the full (rather than fitted) distributions yields smaller values of 0.66 ± 0.06 (i.e., the 90% confidence interval), 0.78 ± 0.03, and 0.73 ± 0.07. For comparison, the cubic phase (I_1) yields $\langle P \rangle = 0.06 \pm 0.09$, consistent with isotropic dye motion. The smaller $\langle P \rangle$ values obtained from the full population in the hexagonal samples (along with disorder depicted by the width of the central peak) reflect the presence of some misaligned micelles, others that incorporate "bends" and regions that produce "isotropic" 2D or 3D diffusion. They may also reflect dynamic fluctuations in micelle alignment. While determination of the exact origins of disorder is left to future work, the uniform distribution of the "misaligned" trajectories (see histogram baseline) suggests that materials disorder results from small defects in the organized micellar phase rather than from large, misaligned domains, as was observed in our previous studies of mesoporous silica.[24]

Interestingly, no clear concentration-dependent trend is observed in the orientation data from the hexagonal phase. Independent repetition of these experiments on a new series of samples also produced no clear trend. It is concluded that at least in the upper ~75% of the hexagonal region of the F127/water/butanol phase diagram, flow induced alignment of the cylindrical micelles is limited by factors other than F127 concentration.

■ CONCLUSIONS

Single molecule tracking and fluorescence correlation spectroscopy methods have been used to probe the influence of mesophase structure on probe molecule diffusion within ternary F127/water/butanol mixtures. The SMT results depict clear 1D diffusion of DTPDI molecules in flow aligned hexagonal mesophases, providing direct, visual evidence that the dye partitions into and diffuses through the hydrophobic micelle core. Diffusion coefficients obtained from SMT were smaller than previously reported and smaller than observed in FCS studies, likely reflective of variations in micelle core microviscosity. FCS data show clear evidence for two component diffusion in hexagonal and cubic mesophases, indicative of the individual roles played by the micelle core and corona in governing molecular diffusion. Trajectory angle analysis data from flow aligned hexagonal samples demonstrates that the incorporated cylindrical micelles are highly ordered. Micelle disorder is concluded to result from local gel defects rather than by the appearance of large misaligned micelle domains.

■ ASSOCIATED CONTENT

ⓢ Supporting Information. Wide-field fluorescence videos and trajectory data from a cubic phase sample. This material is available free of charge via the Internet at http://pubs.acs.org.

■ AUTHOR INFORMATION

Corresponding Author
*E-mail: higgins@ksu.edu.

■ ACKNOWLEDGMENT

■ REFERENCES

(1) Schmidt, T.; Schuetz, G. J.; Baumgartner, W.; Gruber, H. J.; Schindler, H. *Proc. Natl. Acad. Sci. U.S.A.* **1996**, *93*, 2926–2929.

(2) Schuetz, G. J.; Schindler, H.; Schmidt, T. *Biophys. J.* **1997**, *73*, 1073–1080.

(3) Nishimura, S. Y.; Lord, S. J.; Klein, L. O.; Willets, K. A.; He, M.; Lu, Z.; Twieg, R. J.; Moerner, W. E. *J. Phys. Chem. B* **2006**, *110*, 8151–8157.

(4) Ke, P. C.; Naumann, C. A. *Langmuir* **2001**, *17*, 5076–5081.

(5) Ke, P. C.; Naumann, C. A. *Langmuir* **2001**, *17*, 3727–3733.

(6) Deverall, M. A.; Gindl, E.; Sinner, E.-K.; Besir, H.; Ruehe, J.; Saxton, M. J.; Naumann, C. A. *Biophys. J.* **2005**, *88*, 1875–1886.

(7) Honciuc, A.; Howard, A. L.; Schwartz, D. K. *J. Phys. Chem. C* **2009**, *113*, 2078–2081.

(8) Honciuc, A.; Harant, A. W.; Schwartz, D. K. *Langmuir* **2008**, *24*, 6562–6566.

(9) Zhong, Z.; Lowry, M.; Wang, G.; Geng, L. *Anal. Chem.* **2005**, *77*, 2303–2310.

(10) Walder, R.; Schwartz, D. K. *Langmuir* **2010**, *26*, 13364–13367.

(11) Wirth, M. J.; Swinton, D. J.; Ludes, M. D. *J. Phys. Chem. B* **2003**, *107*, 6258–6268.

(12) Wirth, M. J.; Swinton, D. J. *Anal. Chem.* **1998**, *70*, 5264–5271.

(13) Wirth, M. J.; Swinton, D. J. *J. Phys. Chem. B* **2001**, *105*, 1472–1477.

(14) Reznik, C.; Estillore, N.; Advincula, R. C.; Landes, C. F. *J. Phys. Chem. B* **2009**, *113*, 14611–14618.

(15) Kirstein, J.; Platschek, B.; Jung, C.; Brown, R.; Bein, T.; Braeuchle, C. *Nat. Mater.* **2007**, *6*, 303–310.

(16) Zuerner, A.; Kirstein, J.; Doeblinger, M.; Braeuchle, C.; Bein, T. *Nature* **2007**, *450*, 705–709.

(17) Hellriegel, C.; Kirstein, J.; Braeuchle, C.; Latour, V.; Pigot, T.; Olivier, R.; Lacombe, S.; Brown, R.; Guieu, V.; Payrastre, C.; Izquierdo, A.; Mocho, P. *J. Phys. Chem. B* **2004**, *108*, 14699–14709.

(18) Hellriegel, C.; Kirstein, J.; Braeuchle, C. *New J. Phys.* **2005**, *7*, 1–14.

(19) Ito, S.; Fukuya, S.; Kusumi, T.; Ishibashi, Y.; Miyasaka, H.; Goto, Y.; Ikai, M.; Tani, T.; Inagaki, S. *J. Phys. Chem. C* **2009**, *113*, 11884–11891.

(20) Kennard, R.; DeSisto, W. J.; Giririjan, T. P.; Mason, M. D. *J. Chem. Phys.* **2008**, *128*, 134710.

(21) McCain, K. S.; Hanley, D. C.; Harris, J. M. *Anal. Chem.* **2003**, *75*, 4351–4359.

(22) Mahurin, S. M.; Dai, S.; Barnes, M. D. *J. Phys. Chem. B* **2003**, *107*, 13336–13340.

(23) Ye, F.; Collinson, M. M.; Higgins, D. A. *Phys. Chem. Chem. Phys.* **2009**, *11*, 66–82.

(24) Tran Ba, K. H.; Everett, T. A.; Ito, T.; Higgins, D. A. *Phys. Chem. Chem. Phys.* **2011**, *13*, 1827–1835.

(25) Dickson, R. M.; Norris, D. J.; Tzeng, Y.-L.; Moerner, W. E. *Science* **1996**, *274*, 966–969.

(26) Michelman-Ribeiro, A.; Boukari, H.; Nossal, R.; Horkay, F. *Macromolecules* **2004**, *37*, 10212–10214.

(27) Werley, C. A.; Moerner, W. E. *J. Phys. Chem. B* **2006**, *110*, 18939–18944.

(28) Kawai, T.; Yoshinhara, S.; Iwata, Y.; Fukaminato, T.; Irie, M. *ChemPhysChem* **2004**, *5*, 1606–1609.

(29) Schulz, B.; Tauber, D.; Friedriszik, F.; Graff, H.; Schusterz, J.; von Borczyskowski, C. *Phys. Chem. Chem. Phys.* **2010**, *12*, 11555–11564.

(30) Saxton, M. J. *Biophys. J.* **1993**, *64*, 1766–1780.

(31) Jung, C.; Kirstein, J.; Platschek, B.; Bein, T.; Budde, M.; Frank, I.; Muellen, K.; Michaelis, J.; Braeuchle, C. *J. Am. Chem. Soc.* **2008**, *130*, 1638–1648.

(32) Tolbert, S. H.; Firouzi, A.; Stucky, G. D.; Chmelka, B. F. *Science* **1997**, *278*, 264–268.

(33) Melosh, N. A.; Davidson, P.; Feng, P.; Pine, D. J.; Chmelka, B. F. *J. Am. Chem. Soc.* **2001**, *123*, 1240–1241.

(34) Miyata, H.; Noma, T.; Watanabe, M.; Kuroda, K. *Chem. Mater.* **2002**, *14*, 766–772.

(35) Miyata, H. *Microporous Mesoporous Mater.* **2007**, *101*, 296–302.

(36) Constantin, D.; Oswald, P. *Phys. Rev. Lett.* **2000**, *85*, 4297–4300.

(37) Constantin, D.; Oswald, P.; Imperor-Clerc, M.; Davidson, P.; Sotta, P. *J. Phys. Chem. B* **2001**, *105*, 668–673.

(38) Jeon, S.; Granick, S.; Kwon, K.-W.; Char, K. *J. Polym. Sci., Part B* **2002**, *40*, 2883–2888.

(39) Ghosh, S.; Mandal, U.; Adhikari, A.; Bhattacharyya, K. *Chem. Asian J.* **2009**, *4*, 948–954.

(40) Holmqvist, P.; Alexandris, P.; Lindman, B. *J. Phys. Chem. B* **1998**, *102*, 1149–1158.

(41) Nivaggioli, T.; Alexandris, P.; Hatton, T. A.; Yekta, A.; Winnik, M. A. *Langmuir* **1995**, *11*, 730–737.

(42) Escobar-Chavez, J. J.; Lopez-Cervantes, M.; Naik, A.; Kalia, Y. N.; Quintanar-Guerrero, D.; Ganem-Quintanar, A. *J. Pharm. Pharm. Sci.* **2006**, *9*, 339–358.

(43) Alexandris, P.; Athanassiou, V.; Hatton, T. A. *Langmuir* **1995**, *11*, 2442–2450.

(44) Imperor-Clerc, M.; Davidson, P. *Eur. Phys. J. B* **1999**, *9*, 93–104.

(45) Imperor-Clerc, M.; Hamley, I. W.; Davidson, P. *Macromolecules* **2001**, *34*, 3503–3506.

(46) Nivaggioli, T.; Tsao, B.; Alexandris, P.; Hatton, T. A. *Langmuir* **1995**, *11*, 119–126.

(47) Mortensen, K.; Talmon, Y. *Macromolecules* **1995**, *28*, 8829–8834.

(48) Prud'homme, R. K.; Wu, G.; Schneider, D. K. *Langmuir* **1996**, *12*, 4651–4659.

(49) Jiang, J.; Burger, C.; Li, C.; Li, J.; Lin, M. Y.; Colby, R. H.; Rafailovich, M. H.; Sokolov, J. C. *Macromolecules* **2007**, *40*, 4016–4022.

(50) Walderhaug, H.; Nystroem, B. *J. Phys. Chem. B* **1997**, *101*, 1524–1528.

(51) Cau, F.; Lacelle, S. *Macromolecules* **1996**, *29*, 170–178.

(52) Wanka, G.; Hoffmann, H.; Ulbricht, W. *Macromolecules* **1994**, *27*, 4145–4159.

(53) Shiraishi, Y.; Inoue, T.; Hirai, T. *Langmuir* **2010**, *26*, 17505–17512.

(54) Wan, F.; Zhang, J.; Lau, A.; Tan, S.; Burger, C.; Chu, B. *Electrophoresis* **2008**, *29*, 4704–4713.

(55) Harada, A.; Kataoka, K. *Prog. Polym. Sci.* **2006**, *31*, 949–982.

(56) Levy, G. Particle Tracker, 2009; http://rsb.info.nih.gov/ij/.

(57) Wang, H.; Bardo, A. M.; Collinson, M. M.; Higgins, D. A. *J. Phys. Chem. B* **1998**, *102*, 7231–7237.

(58) Moerner, W. E.; Fromm, D. P. *Rev. Sci. Instrum.* **2003**, *74*, 3597–3619.

(59) Grant, C. D.; Steege, K. E.; Bunagan, M. R.; Castner, E. W. *J. Phys. Chem. B* **2005**, *109*, 22273–22284.

(60) Saxton, M. J. *Biophys. J.* **1997**, *72*, 1744–1753.

(61) Qian, H.; Sheetz, M. P.; Elson, E. L. *Biophys. J.* **1991**, *60*, 910–921.

(62) Seebacher, C.; Hellriegel, C.; Deeg, F.-W.; Braeuchle, C.; Altmaier, S.; Behrens, P.; Muellen, K. *J. Phys. Chem. B* **2002**, *106*, 5591–5595.

(63) Elson, E. L.; Magde, D. *Biopolymers* **1974**, *13*, 1–27.

(64) Deming, W. E. *Statistical Adjustment of Data*; Wiley: New York, 1943.

(65) Hood, K.; Nix, B. A. J.; Iles, T. C. *Statistician* **1999**, *48*, 477–493.

(66) Dunn, G. *Statistical Evaluation of Measurement Errors: Design and Analysis of Reliability Studies*; Arnold: London, 2004.

(67) de Gennes, P. G.; Prost, J. *The Physics of Liquid Crystals*; Oxford University Press: New York, 1995.

12743

dx.doi.org/10.1021/jp208234b |*J. Phys. Chem. B* 2011, 115, 12736–12743